MD simulation of steady shock-wave fronts with phase transition in single-crystal iron

V. V. Zhakhovsky, K. P. Migdal, N. A. Inogamov, and S. I. Anisimov

MD simulation of steady shock-wave fronts with phase transition in single-crystal iron

V. V. Zhakhovsky[1,a)], K. P. Migdal[1], N. A. Inogamov[2] and S. I. Anisimov[2]

[1]*Dukhov Research Institute of Automatics, ROSATOM, Moscow 127055, Russia*
[2]*Landau Institute for Theoretical Physics, Russian Academy of Sciences, Chernogolovka, Russia*

a)6asi1z@gmail.com

Abstract. Overdriven shock waves propagating in main crystallographic directions of single-crystal *bcc* iron were studied with moving-window molecular dynamics (MD) technique. To simulate correctly the shock-induced bcc-to-hcp phase transition in iron a new EAM potential fitted to the cold pressure curves and pressure transition at 13 GPa was developed with the stress matching method. We demonstrate that structure of shock fronts depends on orientation of crystal. A peculiar structure of steady shock-wave front in [100] direction is observed. While the ultra-fast $\alpha \to \epsilon$ transition initiated in uniaxially compressed crystal along [100] in elastic zone transforms *bcc* completely to *hcp* phase, transformation in other directions is performed only partially with production of metastable composition of nanometer-sized bcc-hcp-fcc grains.

INTRODUCTION

Fast growth of available number of processors in computational clusters during last decade made feasible atomistic molecular dynamics (MD) simulation of micrometer-sized samples, which approaches a spatial scale in experiments with laser-induced generation of shock wave (SW) in films having thickness of few micrometers. Thus, planning and analysis of experiments in shock-wave physics can be performed directly with MD simulation. Nowadays the various shock-induced phenomena, including elastic-plastic transformation and phase transitions in material under very high-rate deformation, can be studied in detail on atomistic scale during several nanoseconds [1–10].

The success of MD simulation of high-strain-rate phenomena strongly depends on the availability of reliable interatomic potentials that are capable of describing the materials response to an extreme stress gradient of 1 GPa/nm within a shock front, as well as the following shock-induced transformation and relaxation of material in after-shock flow. Reliable MD simulation of polymorphic solid-solid phase transition in iron is of particular interest because such transition is found to be sensitive to duration of loading in laser-induced SW studied in recent experiments [11–13].

In this short report we present a newly developed EAM potential using the stress-matching method [6]. In addition to cold pressure curves the new potential is also specifically fitted to the pressure thresholds of bcc-to-hcp and bcc-to-fcc phase transitions in iron, that distinguishes it from almost all other Fe potentials reviewed and compared extensively in [14]. Using the new potential we study structures of overdriven steady SW in perfect iron crystals with the help of moving window (MW-MD) technique [8, 15]. Structure of ultra-short shock waves in iron studied in experimental research and MD simulation of iron response to femtosecond laser irradiation is discussed in [12].

DEVELOPMENT of EAM POTENTIAL for IRON

There are two well-known methods for development of new interatomic potentials using energy-matching [19–22] or force-matching [23] fitting of potential coefficients, respectively. For energy-matching method the fitting database of *ab initio* calculated energies is built for a large set of atomic configurations. Similarly, a database of *ab initio* calculated forces is used in force-matching method. A mixed method using a combined energy-force database can be also employed. The root problem of such methods lies in the fact that the chosen atomic configurations are not

TABLE 1. Experimental and *ab initio* properties of iron in comparison with calculated ones using a newly-developed EAM potential.

|	Experiment or DFT	Present EAM
Lattice constant a_0 (nm)	0.2858	0.28574
Lattice constant $a_{T=293}$ (nm)	0.286653	0.286653
Cohesion energy E_0 (kJ/mol)	416.43	420.78
Bulk modulus B_0 (GPa)	177.7	177.8
Elastic constant c_{11} (GPa)	243.	243.4
Elastic constant c_{12} (GPa)	145.	145.0
Elastic constant c_{44} (GPa)	116.	115.8
Vacancy formation E_{vf} (kJ/mol)	172.7	178.0
bcc-to-hcp, $P_{\alpha\to\epsilon}$ (GPa)	14.26	14.26
bcc-to-fcc, $P_{\alpha\to\gamma}$ (GPa)	29.	29.0
Melting point T_m (K)	1811	1790
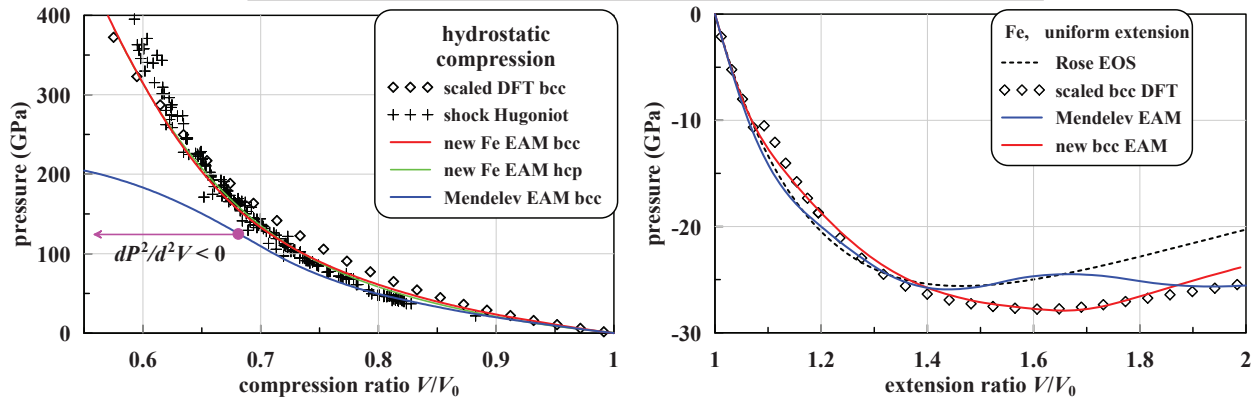
FIGURE 1. Cold pressure curves for hydrostatic compression (left) and stretching (right) of iron. DFT data for *bcc* lattice was not used in fitting procedure above the $\alpha \to \epsilon$ transition at 14.26 GPa. The magenta circle shows an inflection point $\partial^2 P_0/\partial V^2 = 0$, beyond which the sound speed calculated by Mendelev EAM potential [16] drops with compression. Experimental points from shock compression of iron are taken from the shock database [17]. Dashed curve shows pressure from the Rose semi-empirical equation of state Rose [18].

connected by any continuous physical path on the phase diagram of material, like as isothermal or isochoric compression/stretching. Because of number of configurations is usually limited by a few thousands they are greatly separated in multi-dimensional configuration space of multi-atom systems used for building the database. Then, even if an obtained potential is fitted perfectly to the chosen atomic configurations it does not guarantee that a great number of other configurations, which are realized in a continuous physical process but not included in the database, will be reproduced with acceptable accuracy. For such configurations the fitted potential may provide some undesired non-physical response, for instance the increase of compressibility with higher compression of aluminum and nickel simulated by Mishin EAM potentials [21].

Thus, those methods have a common issue in reproducing of cold stresses (along zero-temperature isotherm) as reasonable and smooth functions of uniaxial strain applied to crystal lattice. This issue appears typically at some specific deformations, where the stress may exhibit non-monotonic behavior leading to undesired non-physical effects like to decrease of sound speed with compression or stress oscillation in stretching of crystal along some crystallographic axes as illustrated by blue lines on Fig. 1. The cold $P(V)$ curve obtained by Mendelev EAM potential [16] has an inflection point $\partial^2 P_0/\partial V^2 = 0$ at pressure 120 GPa, after that the sound speed $c_0 = \partial P_0/\partial V = \partial^2 E_0/\partial V^2$ begins to decrease. Such physically unappropriate behavior reduces much the range of applicability of the potential, which is often is ignored in MD simulation of material response to shock loading.

With the aim of developing a potential capable to reproduce correctly the response of iron crystal to deformation in wide range of compression the stress-matching method [6] is used here. The fitting database is built of the stress tensor components $\sigma_{\alpha\beta}(V) = -P_{\alpha\beta}(V)$ calculated by DFT method in cold crystal lattice under continuous hydrostatic and uniaxial deformations. Fitting procedure involves also the constrains of monotonic behavior of $P_{\alpha\alpha}(V)$, including

requirement of increase of sound speed with compression. Because for shock waves with pressure of up to a few hundred GPa in condensed-phase materials the thermal energy and pressure are smaller than the cold energy and pressure taken into account in the stress-matching fitting we can state with assurance that the fitted potential gives also a reasonable thermodynamics of simulated material in a wide range of temperatures up to the critical point.

To obtain the first-principles cold pressure curves of iron DFT calculations using the Vienna *ab initio* simulation package (VASP) [24]. Electron wave functions of crystal containing either one atom in *bcc*-type cell or two atoms in *hcp*-type of cell were calculated with PAW psuedopotential [25, 26] with Perdew-Burke-Ernzerhof (PBE) functional [27]. To describe the polymorphic bcc-to-hcp phase transition the highly accurate DFT calculations with energy cutoff 500 eV and number of k-points $21 \times 21 \times 21$ generated according to the Monkhorst-Pack scheme for sampling the Brillouin zone [28] were performed. The valence band $(3d^7 4s^1)$ and the closest occupied band $3p^6$ are both considered as valence in the used PAW psuedopotential chosen from VASP library.

To calculate the uniaxial pressure components, series of stepwise static calculations with relaxation of atom positions were performed for normal strains along the [100], [110], and [111] directions, respectively. The equilibrium crystals at $P = 0$ were found to have size $a = 0.2830$ nm of *bcc*-cell, and $a = 0.247$ nm and $c/a = 1.5805$ nm for *hcp*-cell. Figures 1 and 2 present the calculated cold pressures/stresses with symbols.

Besides the cold pressures the experimental quantities, including normal density, cohesive energy, elastic constants, and energy of vacancy formation, were included in the fitting database. The pressure thresholds of 14.26 GPa for bcc-to-hcp phase transition in single-crystal iron and 29 GPa for nonequilibrium bcc-to-fcc phase transitions [14] were applied in fitting procedure. The additional constrains, including increase of sound speed with compression, and an inequality for enthalpy of formation $H_{fcc} > H_{hcp}$ prohibiting the hcp-to-fcc transition, were used as illustrated by Fig. 3.

We use the high-order rational functions to represent the EAM potential consisting of a pairwise energy, charge density and embedding energy. Fitting of potential coefficients was performed by minimization of target function with the use of downhill simplex algorithm [29, 30] combined with random walk in multidimensional space of fitting coefficients. Figures 1 and

FIGURE 2. Components of pressure tensor $P_{\alpha\beta}(V/V_0)$ for uniaxial compression of *bcc* iron along [111] direction. DFT data (symbols) were calculated by VASP code. Solid line shows the components obtained with our new EAM potential.

FIGURE 3. Enthalpy of formation of *hcp* and *fcc* phase in respect to *bcc* phase calculated by the new EAM potential. Thresholds of phase transitions is satisfied exactly to the prescribed values because they have the highest priority in fitting procedure. The constrain $H_{fcc} > H_{hcp}$ was applied up to 400 GPa.

2 show the cold pressure curves calculated by our new EAM potential. Average relative deviation of the calculated pressure components from DFT data is about 9%. The range of applicability of the new potential is limited by compression ratio of $V/V_0 = 0.5$ and the maximal pressure of 800 GPa (high pressure range is not shown on Figures).

SIMULATION RESULTS

Predictive MD simulation of iron response to shock loading is our main goal in development of the new potential. To verify the potential we calculate the principal shock Hugoniot of iron with the use of moving-window technique [8]. Figure 4 shows the calculated high-pressure Hugoniot for single crystal oriented in [110] direction and experimental
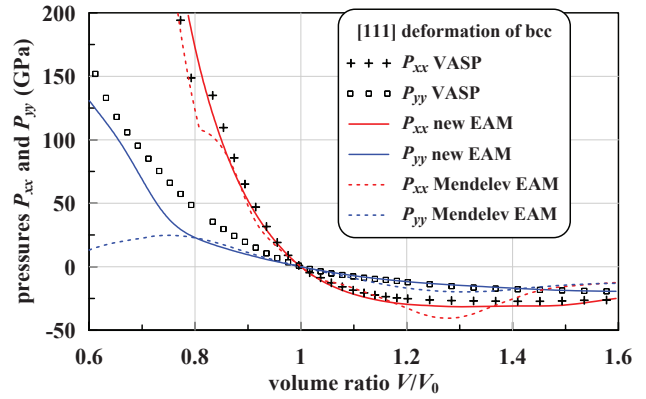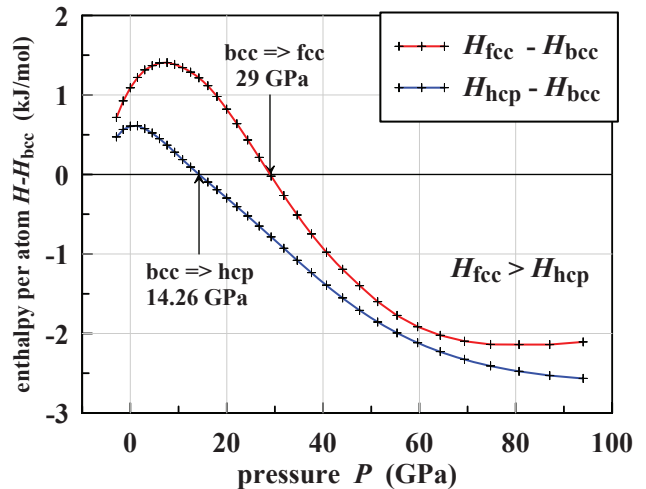
data taken from the shock database [17]. In spite of incompleteness of bcc-to-hcp transition in after-shock motion during several ten picoseconds available in the MW-MD box of 400 nm in length, see discussion of Fig. 6, there is a good agreement between simulated Hugoniot and experimental one. However, the low-pressure Hugoniot for single-crystal iron oriented along [100], where the bcc-to-hcp transition is completed as shown in Fig. 5, lies somewhat higher than the experimental data for polycrystalline sample. This is mostly because the potential gives a slightly higher cold pressure curve of $\epsilon-$ iron in the range of 30-50 GPa. In addition to shock-wave verification the calculated melting point was also in good agreement with the experimental one, see other parameters in Table 1.

To visualize solid and liquid phases of matter during shock-wave simulation the physical parameters like potential energy of atoms, as well as the atomic structure parameters, such as the central-symmetry parameter [31], can be used. However, the gap between potential energies of atoms in solid phases and melt becomes narrow and drift toward higher potential energy with increase of temperature in high-pressure SW. Moreover, the potential energy fluctuation increases much with temperature. The same problem happens with the central-symmetry parameter.

In our simulation the local-order parameters Q_4 and Q_6 introduced by Steinhardt [32, 33] was chosen to probe an atom environment, because it is weakly dependent on temperature and independent on density, and can be calculated fast enough. The family of the angle dependent functions Q_{lm} for a given atom i with nearest neighbors' atoms j having radius vectors $\vec{r}_{ij} = \vec{r}_j - \vec{r}_i$ can be evaluated as

FIGURE 4. Shock Hugoniot from MW-MD simulation of perfect single-crystal iron described by our new EAM potential. Crosses correspond to experimental points taken from the shock-wave database [17].

$$\overline{Q}_{lm}(i) = \left\langle Y_{lm}(\theta(\vec{r}_{ij}), \phi(\vec{r}_{ij})) \right\rangle, \qquad Q_l^2 = \frac{4\pi}{2l+1} \sum_{m=-l}^{l} |\overline{Q}_{lm}|^2, \qquad (1)$$

where Y_{lm} are spherical harmonics, θ and ϕ are the angles of the radius vector (bond) $\vec{r}_{ij}$ measured with respect to some reference coordinate system, and averaging is done among all nearest neighbors selected by Voronoi decomposition. It is important to have a local-order parameter independent from coordinate system and its orientation, so the rotational invariant of second order Q_l shown as second part in Eq. 1. It was demonstrated that such rotational invariants of ranks $l = 4$ and $l = 6$ can be used for analysis of local crystalline structures even in material at high temperatures [34].

To detect the melting transition $l = 6$ is the most suitable rank, because Q_6 has the largest gap between solid and liquid states, and this gap almost does not depend on temperature. But, to distinguish crystalline structures at higher temperatures, where atom distributions in plane Q_4 and Q_6 for particular lattices can overlap, we use atom positions averaged over a short time about 1-2 ps instead of the usage of instantaneous positions in Eq. 1. Such approach reduces much the thermal fluctuation in atom positions, which provides well localized nonoverlapping atom distributions in plane $Q_4 - Q_6$, where *bcc*-like atomic structures are attracted to the coordinates $Q_4^{bcc} = 0.03636965$ and $Q_6^{bcc} = 0.5106882$ of the prefect *bcc* lattice, *hcp* structures – to $Q_4^{hcp} = 0.09722222$ and $Q_6^{hcp} = 0.4847617$, and *fcc* structures are localized around $Q_4^{fcc} = 0.1909407$ and $Q_6^{fcc} = 0.5745243$.

We found that a steady shock in [100] crystallographic direction has a peculiar shock structure because the uniaxial shock loading can easily trigger the $\alpha \rightarrow \epsilon$ transition as shown on Fig. 5. To colorize $Q_4 - Q_6$ blue color is used for *bcc* crystal, green for *hcp*, and red for *fcc* lattice. As it is seen, the $\alpha \rightarrow \epsilon$ transition is initiated for very short time of 3-4 ps within a leading elastic shock front where compression remains uniaxial in [100] direction and shear stress is about 2 GPa. Under such deformation the (110) atomic planes of *bcc* crystal transform to 2D close-packed geometry similar to that in *hcp* lattice. The cooperative shuffle, described in [4], of many those planes produced by the shear stress results in formation of several small-sized pieces of *hcp* phase which later of after-shock flow transform into two large domains as Fig. 5 illustrates. As a result of such fast and "perfect" phase transition the temperature jumps by 90 K from 300 K in the uncompressed $\alpha-$ iron to 390 K in shocked $\epsilon-$ iron. The later formation of larger domains is associated with relatively slow growth of temperature by 40 K within 50 nm after shock front. Increase of transversal period of MD cell leads to increase of domain size but not the number of domains.
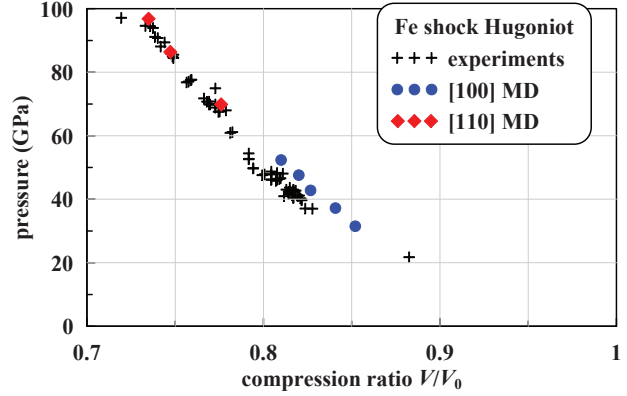
By contrast with shock-wave propagation in [100] direction, the structures of steady shock SW in other directions do not exhibit the completed bcc-to-hcp transition, mostly because the after-shock flow of material is limited by about 250 nm in our MW-MD box. Instead, a composition of nano-sized domains of *bcc*, *hcp* and *fcc* phases is observed in our MD simulations. Figure 6 shows a structure of a SW in iron crystal oriented along [110] direction. Again the phase transitions are initiated in the elastic zone/nose with the shear stress of 7 GPa, but because [110] uniaxial compression cannot generate closed-packed atomic planes from (110) planes of *bcc* crystal the shuffle mechanism of $\alpha \rightarrow \epsilon$ phase transition is not activated here. Thus, a typical two-zone elastic-plastic shock-wave structure is formed in other directions of shock propagation. Uniaxially compressed iron in the elastic nose is plastically transformed to a highly-overcompressed *bcc* phase in the plastic front, which immediately triggers transitions to *hcp* and *fcc* structures independently in many locations. We can see formation of a metastable mixture of all three phases distributed in nanometer-sized grains shown on Fig. 6, but fraction of *fcc* is the smallest one. Our preliminary simulations of SW in other directions indicate that production of different phases depends much on crystal orientation.

As seen such from Fig. 6 the phase composition relaxes slowly in whole available MW-MD computation box, which results in gradual increase of temperature in after-shock flow. It is worth noting that in our MW-MD simulations a relatively low-pressure SW with $P < 60$ GPa moving in [110] direction of perfect iron crystal remains a pure elastic wave without any phase transitions. Thus, the overcompressed crystal can stay in a metastable *bcc* phase at least 100 ps after SW front within about 300 nm path of material flow. Such behavior agrees with recent experimental data obtained for ultra-short SW generated by a femtosecond laser pulse, where $\alpha \rightarrow \epsilon$ phase transition was not detected [12]

CONCLUSION

We developed a new EAM potential for iron, which reproduces correctly not only mechanical response to compression but also bcc-to-hcp and bcc-to-fcc phase transitions. It also provides good description of molten iron, including the surface tension and the melting point which both are very closed to the experimental values.
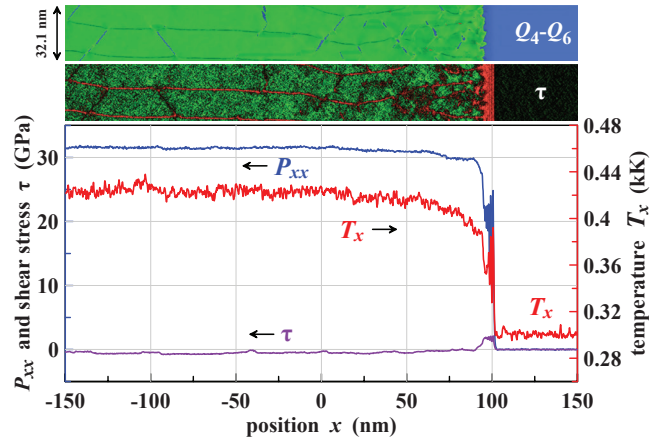

FIGURE 5. Maps of shear stress and combined atomic order parameter $Q_4 - Q_6$ together with component of pressure tensor $P_{xx} \equiv -\sigma_{xx}$ and temperature profiles of SW moving with $u_s = 5.2$ km/s in a single crystal iron oriented in $x = [100]$, where $x-$ axis is a direction of shock-wave propagation. Blue color is used for *bcc* crystal, green for *hcp*, and red corresponds to *fcc* crystal on $Q_4 - Q_6$ map. $\alpha \rightarrow \epsilon$ transition is started just within the elastic nose where the shear stress $\tau = (P_{xx} - (P_{yy} + P_{zz})/2)/2$ is about 2 GPa. Temperature T_x of $x-$ component of atom velocity distribution, which is non-Maxwellian within a shock front, is shown by a red line.
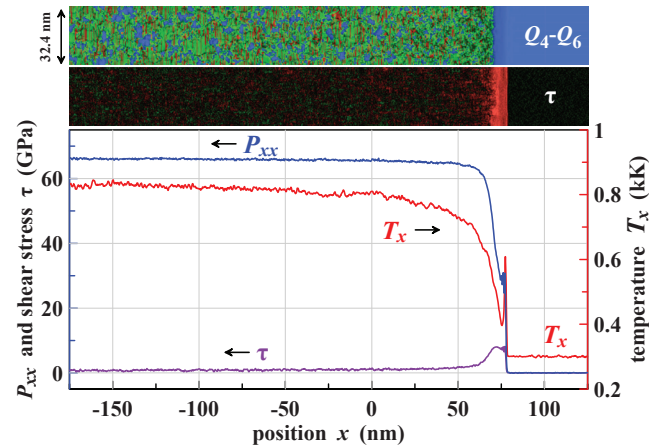

FIGURE 6. Maps of shear stress and combined atomic order parameter $Q_4 - Q_6$ together with pressure tensor component P_{xx} and temperature T_x profiles of SW moving with $u_s = 6.25$ km/s in a single crystal iron oriented in $x = [110]$. Blue color is used for *bcc* crystal, green for *hcp*, and red corresponds to *fcc* crystal on $Q_4 - Q_6$ map. Metastable mixture of nano-sized domains of different phases is formed in bcc-to-hcp and bcc-to-fcc phase transitions initiated after elastic nose with shear stress τ of about 7 GPa. Relaxation of such mixture manifests itself as slow temperature growth in after-shock flow. See other description details in caption to Fig. 5.

The above properties are crucial for predictive MD simulation of shock-wave loading associated with phase transitions. The new potential was successfully used for calculation of shock Hugoniot for iron. We preformed moving-window MD study of steady shock-wave structures propagating in [100] and [110] directions of prefect single crystal

iron. It was found that the [100] oriented crystal exhibits fast $\alpha \to \epsilon$ transition completing for few picoseconds within a shock front because the very efficient shuffle mechanism is realized.

However, in other crystallographic directions the shuffle mechanism is not activated, which leads to shock-induced formation of long-living metastable mixture of small nanometer-sized grains of *hcp*, *bcc*, and *fcc* phases within a plastic shock front. Because such phase mixture slowly relaxes in after-shock flow we suggest that the complete transition to *hcp* solid will require a few hundred picoseconds, which exceeds much the available after-shock time in the used moving-window box of 400 nm in length.

ACKNOWLEDGEMENTS

REFERENCES

[1] E. M. Bringa, J. U. Cazamias, P. Erhart, J. Stölken, N. Tanushev, B. D. Wirth, R. E. Rudd, and M. J. Caturla, J. Appl. Phys. **96**, 3793–3799 (2004).

[2] E. M. Bringa, K. Rosolankova, R. E. Rudd, B. A. Remington, J. S. Wark, M. Duchaineau, D. H. Kalantar, J. Hawreliak, and J. Belak, Nature Materials **5**, 805–809 (2006).

[3] T. C. Germann, J. E. Hammerberg, and B. L. Holian, AIP Conference Proceedings **706**, 285–288 (2004).

[4] K. Kadau, T. C. Germann, P. S. Lomdahl, and B. L. Holian, Phys. Rev. B **72**, p. 064120 (2005).

[5] K. Kadau, J. L. Barber, T. C. Germann, and A. B. J., Phys. Rev. E **78**, p. 045301 (2008), see also LANL report LA-UR-08-2605.

[6] V. V. Zhakhovskii, N. A. Inogamov, Y. V. Petrov, S. I. Ashitkov, and K. Nishihara, Appl. Surf. Sci. **255**, 9592–9596 (2009).

[7] B. Demaske, V. V. Zhakhovsky, N. A. Inogamov, and I. I. Oleynik, Phys. Rev. B **82**, p. 064113 (2010).

[8] V. V. Zhakhovsky, M. M. Budzevich, I. I. Oleynik, and C. T. White, Phys. Rev. Lett. **107**, p. 135502 (2011).

[9] M. M. Budzevich, V. V. Zhakhovsky, C. T. White, and I. I. Oleynik, Phys. Rev. Lett. **109**, p. 125505 (2012).

[10] B. J. Demaske, V. V. Zhakhovsky, N. A. Inogamov, and I. I. Oleynik, Phys. Rev. B **87**, 054109 1–9 (2013).

[11] S. I. Ashitkov, P. S. Komarov, M. B. Agranat, G. I. Kanel', and V. E. Fortov, JETP Lett. **98**, 394–400 (2013).

[12] S. I. Ashitkov, V. V. Zhakhovsky, N. A. Inogamov, P. S. Komarov, M. B. Agranat, and Kanel', AIP Conference Proceedings (2016), in this Proceedings.

[13] J. C. Crowhurst, B. W. Reed, M. R. Armstrong, H. B. Radousky, J. A. Carter, D. C. Swift, J. M. Zaug, R. W. Minich, N. E. Teslich, and M. Kumar, Journal of Applied Physics **115**, p. 113506 (2014).

[14] N. Gunkelmann, E. M. Eduardo, M. Bringa, K. Kang, G. J. Ackland, C. J. Ruestes, and H. M. Urbassek, Phys. Rev. B **86**, p. 144111 (2012).

[15] V. V. Zhakhovskii, K. Nishihara, and S. I. Anisimov, JETP Lett. **66**, 99–105 (1997).

[16] M. I. Mendelev, S. Han, D. J. Srolovitz, G. J. Ackland, D. Y. Sun, and M. Asta, Philos. Mag. **83**, p. 3977 (2003).

[17] Shock wave database: http://teos.ficp.ac.ru/rusbank/.

[18] J. H. Rose, J. R. Smith, F. Guinea, and J. Ferrante, Phys. Rev. B **29**, p. 2963 (1984).

[19] I. J. Robertson, V. Heine, and M. C. Payne, Phys. Rev. Lett. **70**, p. 1944 (1993).

[20] I. J. Robertson, D. I. D. I. Thomson, V. Heine, and M. C. Payne, J. Phys.: Condens. Matter **6**, p. 9963 (1994).

[21] Y. Mishin, D. Farkas, M. J. Mehl, and P. D. A., Phys. Rev. B **59**, p. 3393 (1999).

[22] Y. Mishin, "Interatomic potentials for metals," in *Handbook of Materials Modeling*, Vol. 1, edited by S. Yip (Springer, 2005).

[23] F. Ercolessi and A. J. B., Europhys. Lett. **26**, p. 583 (1994).

[24] G. Kresse and J. Furthmuller, Phys. Rev. B **54**, p. 11169 (1996).

[25] P. E. Blöchl, Phys. Rev. B **50**, p. 17953 (1994).

[26] G. Kresse and J. Joubert, Phys. Rev. B **59**, p. 1758 (1999).

[27] J. P. Perdew, K. Burke, and M. Ernzerhof, Phys. Rev. Lett. **77**, p. 3865 (1996).

[28] H. J. Monkhorst and J. D. Pack, Phys. Rev. B **13**, p. 5188 (1976).

[29] J. A. Nelder and R. Mead, Comp. J. **7**, 308–313 (1965).

[30] W. H. Press, B. P. Flannery, S. A. Teukolsky, and W. T. Vetterling, *Numerical Recipes in FORTRAN: The Art of Scientific Computing. 10.4. Downhill Simplex Method in Multidimensions* (Cambridge University Press, 1992).

[31] C. L. Kelchner, S. J. Plimpton, and J. C. Hamilton, Phys. Rev. B **58**, 11085–11088 (1998).

[32] P. J. Steinhardt, D. R. Nelson, and M. Ronchetti, Phys. Rev. B **28**, 784–805 (1983).

[33] W. Lechner and C. Dellago, J. Chem. Phys. **129**, p. 114707 (2008).

[34] B. A. Klumov, S. A. Khrapak, and G. E. Morfill, Phys. Rev. B **83**, p. 184105 (2011).